Correlated spin canting in ordered core-shell Fe_{3}O_{4}/Mn_{x}Fe_{3−x}O_{4} nanoparticle assemblies

Y. Ijiri, K. L. Krycka, I. Hunt-Isaak, H. Pan, J. Hsieh, J. A. Borchers, J. J. Rhyne, S. D. Oberdick, A. Abdelgawad, and S. A. Majetich

Phys. Rev. B **99**, 094421 — Published 18 March 2019

DOI: 10.1103/PhysRevB.99.094421

Correlated Spin Canting in Ordered Core-Shell $Fe_3O_4/Mn_xFe_{3-x}O_4$ Nanoparticle Assemblies

Y. Ijiri,[1,*] K. L. Krycka,[2] I. Hunt-Isaak,[1] H. Pan,[1] J. Hsieh,[1] J. A. Borchers,[2] J. J. Rhyne,[2] S. D. Oberdick,[3,4] A. Abdelgawad,[3,5] and S. A. Majetich[3]

[1] *Oberlin College, Department of Physics and Astronomy, Oberlin, OH 44074*

[2] *National Institute of Standards and Technology, NIST Center for Neutron Research, Gaithersburg, MD 20899*

[3] *Carnegie Mellon University, Department of Physics, Pittsburgh, PA 15213*

[4] *National Institute of Standards and Technology, Applied Physics Division, Physical Measurement Laboratory, Boulder, CO, 80305*

[5] *Carnegie Mellon University, Department of Materials Science and Engineering, Pittsburgh, PA 15213*

(Dated: March 4, 2019)

Abstract

Polarization-analyzed small-angle neutron scattering methods are used to determine the spin arrangements and experimental length scales of magnetic correlations in ordered three-dimensional assemblies of ~ 7.4 nm diameter core-shell $Fe_3O_4/Mn_xFe_{3-x}O_4$ nanoparticles. In moderate to high magnetic fields, the assemblies display a canted magnetic structure where the canting direction is coherent from nanoparticle to nanoparticle, in contrast to the less extended, more single particle-like behavior for similar ferrite assemblies. The observed magnetic scattering is modeled by assuming that the interparticle dipolar coupling combined with Zeeman effects in a field leads to nanoparticle domains with preferred net spin alignments relative to packing symmetry axes. Over a range of fields and temperatures, the model qualitatively explains the observed scattering anomalies in terms of clusters that vary in area and thickness, highlighting the complex structures adopted in real, dense nanoparticle systems. The clusters often have a strong two-dimensional magnetic character which is attributed to structural stacking faults and the resulting influence of interparticle dipolar interactions for these magnetically soft nanoparticles.

I. I. INTRODUCTION

Magnetic oxide nanoparticles are central to many applications ranging from ultra-dense data storage to medical diagnostics and cancer therapy[1–3]. Due to the biocompatibility of manganese, particular attention has been paid to tailoring manganese ferrite nanoparticles, often through the addition of a core-shell geometry with distinct yet coupled components[4–6]. While magnetic properties like saturation magnetization and coercivity can be made to differ from the bulk, it has been difficult to pinpoint the specific underlying mechanisms responsible for the changes or even to fully characterize the spin structures involved.

In recent work, we have shown that dense collections of core-shell $Fe_3O_4/Mn_xFe_{3-x}O_4$ nanoparticles[7] can have significant canting of spins within each nanoparticle as opposed to the simply parallel and antiparallel arrangements expected for ferrite spinel structures. Furthermore, the canted spin arrangement from nanoparticle to nanoparticle can be coherent over significant length scales, in contrast to the behavior of simpler systems such as $CoFe_2O_4$ or Fe_3O_4 dense assemblies in which the non-collinear spins within a nanoparticle show either no correlation or only limited correlation to neighboring particles[8–10].

From the bulk behavior of these oxides, we expect manganese ferrite assemblies to present an interesting test case for understanding spin structures. While the saturation magnetization for $MnFe_2O_4$ is comparable to $CoFe_2O_4$ or Fe_3O_4, the bulk ordering temperature for $MnFe_2O_4$ is roughly 200-250 K lower, indicating weaker exchange interactions, with magnetocrystalline anisotropy also reduced[11]. On the other hand, given the non-magnetic organic surfactant that is used to physically separate these nanoparticles, it is most likely that dipole-dipole interactions remain important for the coherent magnetic structures observed, over other competing energy terms.

While long studied, dipolar interactions are of broad interest today in a range of research spanning from artificial spin ices[12] to collections of Rydberg atoms[13]. More closely related to the current work on nanoparticles, recent micromagnetic simulations reveal the possible anisotropic spin-misalignment correlations that might emerge in a porous iron ferromagnet due to dipolar effects[14]. Dipolar interactions were also critical in Monte Carlo simulations guided by magnetometry data, probing the crossover from two dimensional (2D) to three-dimensional (3D) magnetic behavior in ordered collections of γ-Fe_2O_3 nanoparticles[15]. More recent work on disordered, agglomerated clusters of iron oxide nanoparticles has revealed a

tendency for anti-parallel alignment from dipolar coupling[16]. From an applications standpoint, dipolar interactions between nanoparticles are being investigated for the resulting effects on hyperthermia[17,18] as well as for the collective domain structures formed from nanoparticle aggregation *in vivo*[19]. This context motivates additional study of such interactions, particularly in well-characterized, controlled systems of nanoparticles.

Small angle neutron scattering with either partial or full polarization analysis has been shown to be a very effective probe of magnetic ordering for powdered collections of nanoparticles[5,7–10,16,20–27]. Here, we test further the nature of the interparticle magnetic correlations in ordered core-shell $Fe_3O_4/Mn_xFe_{3-x}O_4$ nanoparticle assemblies, making extensive use of full polarization-analyzed small-angle neutron scattering (PASANS) techniques[28–30] to characterize extensively the magnetic scattering over a range of field and temperature conditions. Two key features are noted: (1) an interparticle magnetic diffraction peak with significant components of magnetic ordering *both* parallel and perpendicular to an applied magnetic field and (2) an angle-dependent magnetic scattering component which varies as well with scattering vector. The results are interpreted in terms of a model consisting of plate-like magnetic clusters of close-packed nanoparticles with in-plane easy symmetry axes and possible long-range correlations amongst particle magnetic moments. The net magnetization direction of a given cluster is determined by a balance of dipolar and Zeeman energy considerations, with moments preferentially oriented near easy symmetry axis directions of the packed arrays that are closest to an applied magnetic field direction. Though the nanoparticles self-assemble into large three-dimensional structures, the coherent magnetic domains have a strong two-dimensional character reflecting the sensitivity of the dipolar interactions to local structural disorder such as stacking faults. The data highlight the complexity of magnetic structures in dense nanoparticle assemblies and the importance of sensitive experimental probes.

II. II. EXPERIMENTAL AND DATA ANALYSIS PROCEDURES

The $Fe_3O_4/Mn_xFe_{3-x}O_4$ nanoparticles for this investigation were prepared by high temperature, non-aqueous solution chemistry methods as described previously, with oleic acid as the surfactant to prevent particle agglomeration[5]. Due to the large difference in the decomposition temperature of the iron and manganese precursor materials, the particles had

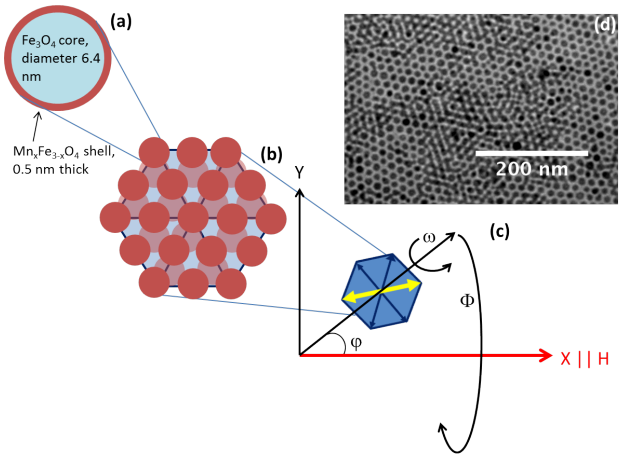

FIG. 1. (Color online.) (a) Schematic of the composition of the core-shell nanoparticles, (b) organized into face-centered cubic close-packed clusters for magnetic modeling, (c) each with different possible orientation (indicated by angles ψ, ω, and Φ) relative to an applied field along X (in red). Arrows within the depicted close-packed region in (c) denote expected six-fold easy symmetry axes; the thicker (yellow) pair indicate the set closest to the applied field direction in this instance. The stacking of the layers is FCC to match the observed structural ordering. The direction of magnetization $\vec{M}$ is determined in the model by the energy minimum between alignment in the plane (black or yellow arrows) and along the field direction (red arrow). Inset (d) shows a TEM image of self-assembled monolayers and bilayers of the nanoparticles and the presence of dislocations and faults in the ordering.

an iron-rich core and a manganese and iron containing shell, as sketched in Fig. 1(a). Specifically, they were best described as having a total mean particle diameter of 7.4 nm $\pm$ 1.0 nm with a shell of thickness $\approx$ 0.5 nm and a chemical composition of $Fe_3O_4/Mn_xFe_{3-x}O_4$ where x is approximately one, based on high-resolution transmission electron microscopy (HR-TEM), x-ray absorption spectroscopy, x-ray magnetic circular dichroism, and Mössbauer data[7].

Through a combination of alcohols with different solubilities for the particles[31,32], the nanoparticles were self-assembled into dense arrays with an apparent close-packed face-centered cubic (FCC) stacking, as determined in previous work on related particles[33,34]; no applied magnetic field was used in the crystal formation process. The dense arrays of nanoparticles were sealed in aluminum cells for neutron scattering measurements. As measured by scanning electron microscopy, the characteristic length scale of an assembled

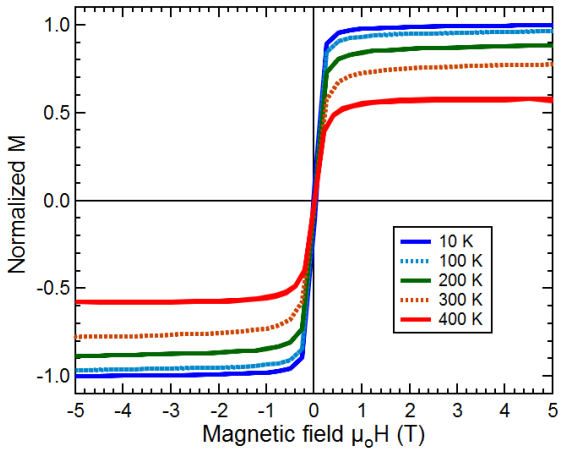

FIG. 2. (Color online.) Comparison of magnetization curves for the dense assemblies of nanoparticles at 10 K (dark blue), 100 K (light blue), 200 K (green), 300 K (orange), and 400 K (red). Since an absolute mass normalization is not feasible due to the unknown amount of included surfactant content, the data are normalized against the 10 K maximum value at 5 T.

nanocrystal was $\approx$ 10 μm, with a $\approx$ 1 μm structural domain or coherence size, given the tendency to form stacking faults and dislocations in the assembly process. A TEM image of monolayers and bilayers of the particles (Fig. 1 (d)) illustrates the nature of the structural ordering, with Fig. 1(b) and (c) sketching a partial arrangement used to model the magnetic characteristics as discussed in Section IV. Standard magnetization measurements versus applied field (depicted in Figure 2) were taken using a superconducting quantum interference device (SQUID) magnetometer at temperatures ranging from 10 K to 400 K to confirm the overall magnetic behavior and to guide neutron scattering measurements.

PASANS experiments were performed at the NIST Center for Neutron Research using the NG7 SANS instrument, an in-beam FeSi supermirror polarizer cavity to polarize the incident neutrons, a radio frequency (RF) spin flipper to switch the polarization of the incident neutrons, and a polarized ^{3}He cell in transmission geometry as a spin analyzer equipped with an in-situ NMR flipper for the scattered neutrons as described in earlier work[35,36]. The sample temperature was adjusted in a closed-cycle He refrigerator from 10-400 K, and an electromagnet was used to apply magnetic fields ($\mu_o H$) up to 1.5 T, which for these dense arrays of nanoparticles yield magnetization values that are very close to ($\sim$ 97-99% of) the observed saturation values at 5 T shown in Fig. 2. Data were collected in

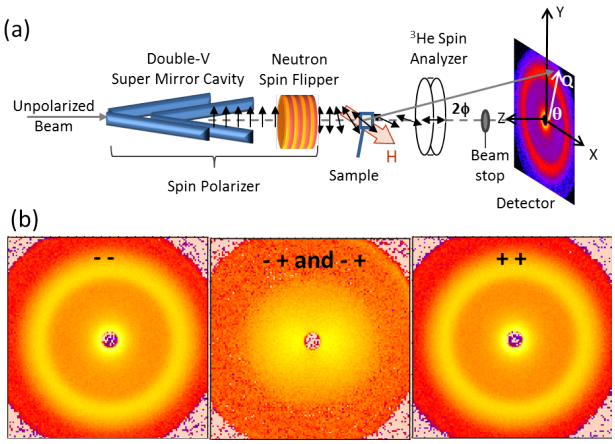

FIG. 3. (Color online.)(a) Experimental setup includes a polarizing supermirror and RF flipper to select the incident spin state and a ^{3}He cell with in-situ NMR flipper to select the scattered spin state. The angle θ shown is between the X axis and the projection of $\vec{Q}$ onto the $X-Y$ plane. The scattering pattern is collected on a 2D detector with (b) showing polarization-corrected images for the $Fe_3O_4/Mn_xFe_{3-x}O_4$ nanoparticles at 400 K in a small remanent field. The I^{+-} and I^{-+} patterns have been added together.

transmission with a two-dimensional (2D) detector at two different distances to span the scattering vector $\vec{Q}$ range from ≈ 0.01 Å^{-1} to 0.15 Å^{-1}. Figure 3(a) illustrates the set-up with the neutron beam along Z, the applied field along X, the detector in the $X-Y$ plane, and the angle θ between $\vec{Q}$ and X. Note that the magnitude of $|\vec{Q}|= 4\pi \sin(\phi)/\lambda$, with 2ϕ, the scattering angle between source and detector and λ, neutron wavelength.

Corrections for the time-dependent decay of the ^{3}He polarization, inefficiencies in the supermirror and flippers, and detector inhomogeneities were made, and the data were reduced following procedures outlined previously[29,37]. As described in the supplemental material[38], particular attention was taken to account for sample depolarization and to match the degree of polarization correction in the vicinity of an observed magnetic Bragg reflection to that seen in lower Q scattering regions. With the direction of the neutron spin relative to the polarization axis denoted as + or -, applying these corrections then yielded the intensity measurements of all four neutron spin cross-sections (I^{++}, I^{--}, I^{+-}, and I^{-+}) corresponding to either initially + or - spin state neutrons scattering into + or - neutrons. Examples of the corrected 2D SANS images are shown in Fig. 3(b) for the sample at 400 K and a small remanent field (≈ 0.005 T) which approximates true zero[39].

The corrected scattering intensities I for the four different polarization conditions are proportional to squared combinations of the nuclear and magnetic structure factor of the sample, taking into consideration the individual scattering strength of the nanoparticles as well as the directional dependence of the neutron interaction with magnetic moments[28,29]. Since the sample is macroscopic, the nuclear component can be represented by a single isotropic spatial Fourier transform N,

$$N(\vec{Q}) \equiv \sum_{n=K} \rho_N(K) exp(i\vec{Q} \cdot \vec{R_K}), \tag{1}$$

with ρ_N the structural scattering length density, and $\vec{R_K}$, the relative position of the Kth scatterer. Similarly, the magnetic analogues, M_X, M_Y, and M_Z, can be written in general as

$$M_J(\vec{Q}) \equiv \sum_{n=K} \rho_{M_J}(K) exp(i\vec{Q} \cdot \vec{R_K}), \tag{2}$$

with J either X, Y, or Z, and ρ_J, the appropriate magnetic scattering length density.

While the expressions to isolate components can be quite complex, they simplify for the geometry depicted in Fig. 3(a) and certain key angles and assumptions[29]. Again, since the sample consists of crystalline grains of close-packed nanoparticles, but with no distinct orientation from grain to grain, the structural component can be extracted simply from a portion of the non-spin flip (NSF) scattering intensities:

$$N^2 \equiv |N(Q)|^2 = I^{++}_{\theta=0^\circ} + I^{--}_{\theta=0^\circ}, \tag{3}$$

using area-normalized sector slices of $\pm 10^\circ$ taken from $\theta = 0^\circ$, e.g. along the field direction X as indicated in Fig. 3(a).

As a result of the selection rules, the magnetic Fourier component M_X can be extracted rather generally from:

$$M_X^2 \equiv |M_X(\vec{Q}, 90^\circ)|^2 = I^{++}_{\theta=90^\circ} + I^{--}_{\theta=90^\circ} - |N(Q)|^2, \tag{4}$$

using data for $\theta = 90^\circ$, e.g along the Y direction. However, the statistical uncertainties associated with Eqn. 4 can be quite large, particularly if the structural component N is much larger than the magnetic ones. Alternatively, the portion of this magnetic Fourier component in phase with the structural scattering can be computed from the NSF data, using:

$$M^2_{X,net} \equiv |M_{X,net}(\vec{Q}, 90^\circ)|^2 = \frac{|I^{--}_{\theta=\pm 90^\circ} - I^{++}_{\theta=\pm 90^\circ}|^2}{4N^2}. \tag{5}$$

In this case, the PASANS extracted intensity is sensitive to only the *net* magnetization along the field direction, as opposed to the total magnetization or magnetic regions both parallel and antiparallel to the field for the expression in Eqn. 4. For large magnetic fields where the correlation between M_X and N is expected to be complete, Eqns. 4 and 5 have been shown to yield identical results[29], but with smaller uncertainties for Eqn. 5.

The spin flip (SF) scattering data are particularly rich in information on the magnetic Fourier transform components. In general, the two spin flip cross-sections summed together, $I_{SF}(\vec{Q},\theta) = I^{+-}(\vec{Q},\theta) + I^{-+}(\vec{Q},\theta)$, yield

$$\begin{aligned} I_{SF}(\vec{Q},\theta) \equiv |M_X(\vec{Q},\theta)|^2 sin^2(\theta)cos^2(\theta) + |M_Z(\vec{Q},\theta)|^2 \\ -2|M_X(\vec{Q},\theta)||M_Y(\vec{Q},\theta)|sin(\theta)cos^3(\theta)\overline{cos}(\delta\psi_{M_X,M_Y}) \\ +|M_Y(\vec{Q},\theta)|^2 cos^4(\theta), \end{aligned} \tag{6}$$

which has a term involving an interference phase factor $\delta\psi$ between the M_X and M_Y components, averaged over the neutron spatial coherence length. Note that for $\theta = 90°$, then Eqn. 6 simplifies to yield

$$I_{SF}(\vec{Q},90°) = M_Z^2(\vec{Q},90°) \equiv M_Z^2. \tag{7}$$

In the case of isotropic, uncorrelated, non-interacting magnetic moments (for which M_X=M_Y=M_Z), as one might expect in remanence, then Eqn. 6 for $\theta = 0°$ can become

$$I_{SF,uncorr}(\vec{Q},0°) = M_Y^2(\vec{Q},0°) + M_Z^2(\vec{Q},0°) \equiv 2M_Z^2, \tag{8}$$

yielding a 2:1 ratio in the SF intensities. However, in general, with the presence of interactions and extended magnetic structures, the SF ratio defined as

$$SFR \equiv \frac{I_{SF}(\vec{Q},0°)}{I_{SF}(\vec{Q},90°)} \tag{9}$$

may deviate significantly from two, as observed in the case of dense Fe_3O_4 nanoparticle assemblies[10].

III. III. EXPERIMENTAL RESULTS

As is apparent from Fig. 3(b), the dominant structural feature in the non-spin flip data for these nanoparticles is a ring of scattering, stemming from structural order that persists over multiple nanoparticles in these dense, self-assembled collections. As shown in the supplementary material[38], for a wide range of field and temperature conditions, this Bragg peak is modeled well by a FCC lattice of nanoparticles with diameter 7.4 nm ± 1 nm and lattice spacing of 12 nm ± 1 nm, with values and standard uncertainties consistent with the TEM results which showed that the particles prior to crystal formation had a mean diameter of 7.0 nm with a standard deviation of 1.4 nm[7]. In the modeling, a 12% deviation in lattice spacing captures the presence of stacking faults and other defects in the structure. The observed FCC nanoparticle structure is consistent with that seen in a range of other dense nanoparticle systems consisting of analogous oxides such as Fe_3O_4[9] and $CoFe_2O_4$[8] or even non-magnetic nanoparticles such as CdSe[31].

While the structural features remain mostly unchanged, Figure 4 depicts the characteristic magnetic signature along the field direction, M_X^2, extracted from Eqn. 4 for the various conditions. In general, for each field value, lower temperature is associated with increased magnetic scattering intensity consistent with the magnetization data in Fig. 2. In remanence, the signal is most evident at low Q, whereas in an applied field, a feature near the Q associated with the structural interparticle peak (Q=0.085$\mathring{A}^{-1}$) becomes prominent. However, in either case, the large statistical uncertainties impede further interpretation.

To clarify the nature of the magnetic scattering component associated with the field direction, we investigate as well the extracted PASANS intensity for $M_{X,net}^2$ assuming coherence of M_X with N, as indicated in Eqn. 5 and depicted in Figure 5. The interparticle peak is now clearly evident; the data show the presence of a field-aligned component over multiple nanoparticles, but with variable intensity as field and temperature are adjusted. $M_{X,net}^2$ is most intense at lower temperatures and higher fields; a significantly smaller, almost negligible signal is observed in the ≈ 0.005 T remanent field of the magnet, with the signal decreasing with increasing temperature as expected for a probe of net magnetization and as expected based on the SQUID magnetometry results (Fig. 2).

In contrast to these data, the data from the SF scattering indicate more clearly a complex magnetic signature, considering M_Z^2, with Z again perpendicular to the applied magnetic

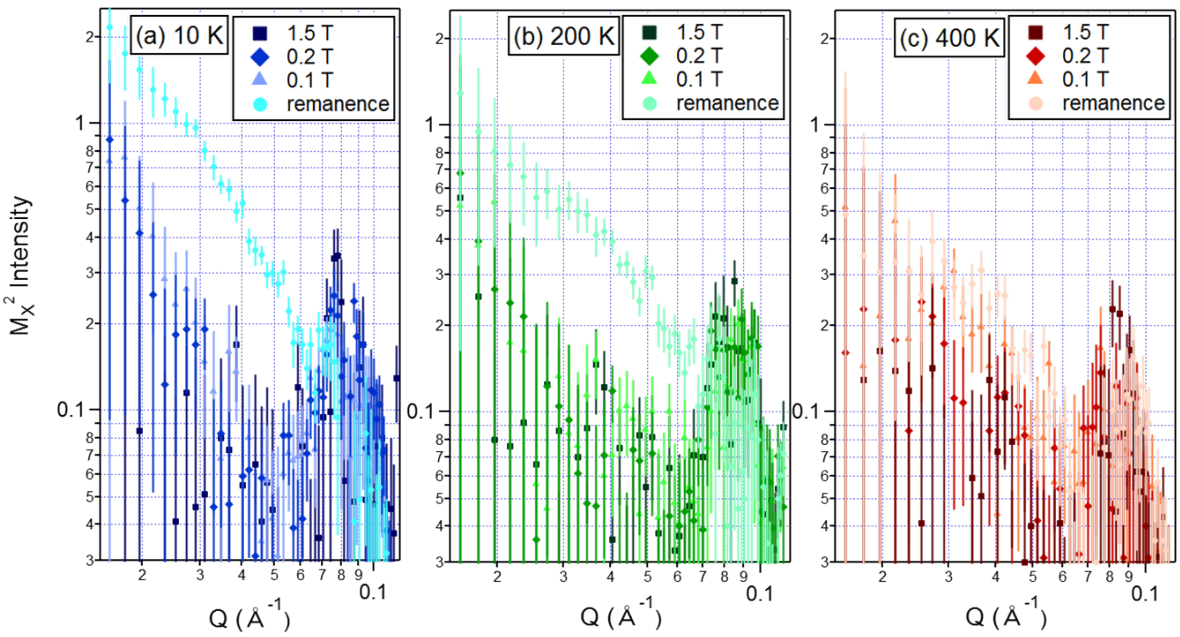

FIG. 4. (Color online.) Data for extracted PASANS intensity M_X^2 using Eqn. 4 vs. scattering vector Q for (a) 10 K (b) 200 K and (c) 400 K with squares for 1.5 T, diamonds for 0.2 T, triangles for 0.1 T, and circles for remanent fields. Error bars in the plot denote standard uncertainties.

field. Figure 6 shows the PASANS intensity M_Z^2 derived from Eqn. 7 as a function of scattering vector Q for a range of fields and temperatures. Note that for a number of sample conditions, the data display an interparticle peak that mimics the structural *and* M_X^2 behavior. The peak is strongest at low temperatures and intermediate magnetic fields. The simultaneous presence of a Bragg reflection in both M_X^2 and M_Z^2 indicates not only spins misaligned with the field in certain conditions, but also the presence of a coherent spin canting across *multiple* nanoparticles, e.g. the formation of extended regions of tilted ordering.

The observed Bragg peak in M_Z^2 contrasts markedly with the behavior seen in other ferrite nanoparticle assemblies. For dense $CoFe_2O_4$ assemblies, this perpendicular magnetic scattering component showed only the form factor of single particle scattering, indicating a tilted magnetic order that was not coherent from nanoparticle to nanoparticle[8]. In the case of Fe_3O_4 ordered assemblies, M_Z^2 showed a large dip, rather than peak near the scattering vector associated with the structural ordering; the magnetic form factor matched to that for shell scattering with only short range correlations extending over a few nanoparticles[9,10].

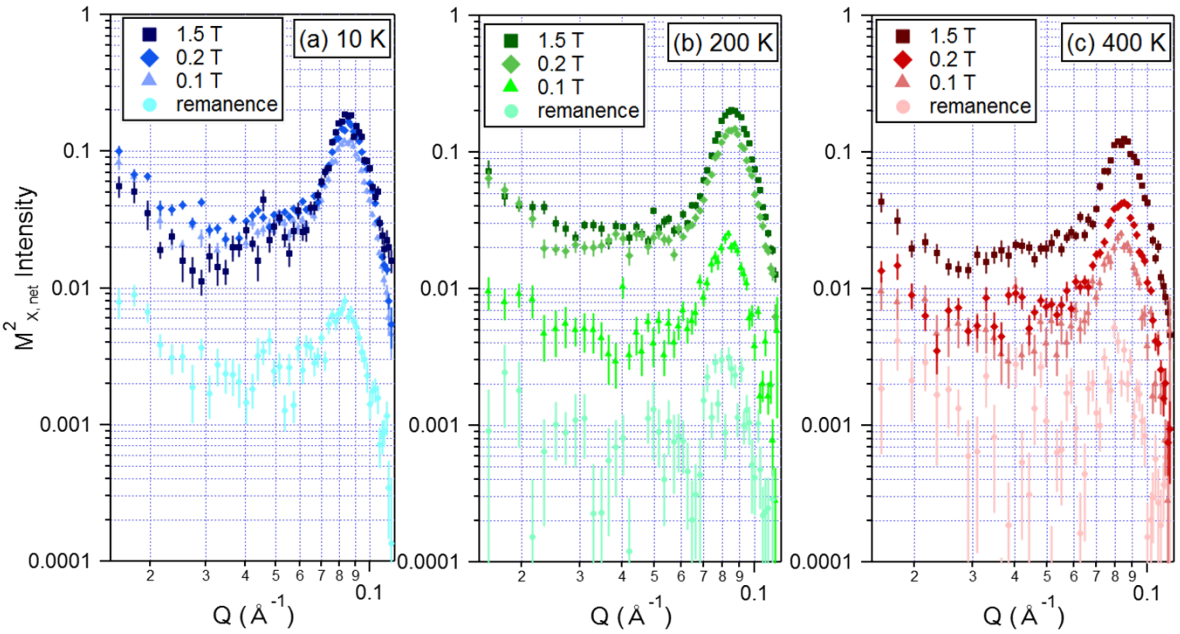

FIG. 5. (Color online.) Data for extracted PASANS intensity $M^2_{X,net}$ using Eqn. 5 vs. scattering vector Q for (a) 10 K (b) 200 K and (c) 400 K with squares for 1.5 T, diamonds for 0.2 T, triangles for 0.1 T, and circles for remanent fields. Error bars in the plot denote standard uncertainties. Relative to Fig. 4, scale is changed to show better features in the data.

Note that in Fig. 6, besides the interparticle reflection, the M^2_Z data indicate additional scattering intensity, particularly at lower Q and for low temperature and field conditions. At high temperatures and in remanence, the shape of the observed scattering is suggestive of a single particle form factor and mimics the magnitude and shape of the falloff seen in M^2_X in Fig. 4(c), as would be expected for uncorrelated, randomized moments. However, detailed fitting is complicated in this instance, given the known chemical core-shell nature of the $Fe_3O_4/Mn_xFe_{3-x}O_4$ nanoparticles here as well as overlapping contribution from any remaining interparticle reflection intensity.

Figure 7 illustrates further the complexity of the spin structures in this system, depicting the spin flip ratio (SFR) of the horizontal SF scattering component (θ=0°) to the vertical component (θ=90°) for the range of experimental conditions. In remanence, the SFR is closest to the expected 2:1 ratio for uncorrelated, isotropic equivalent magnetic moments, whereas in high magnetic field, the extended magnetic structure leads to a SFR closer to 1:1. In detail, at given temperatures and fields, the Q dependence also varies in these assemblies,

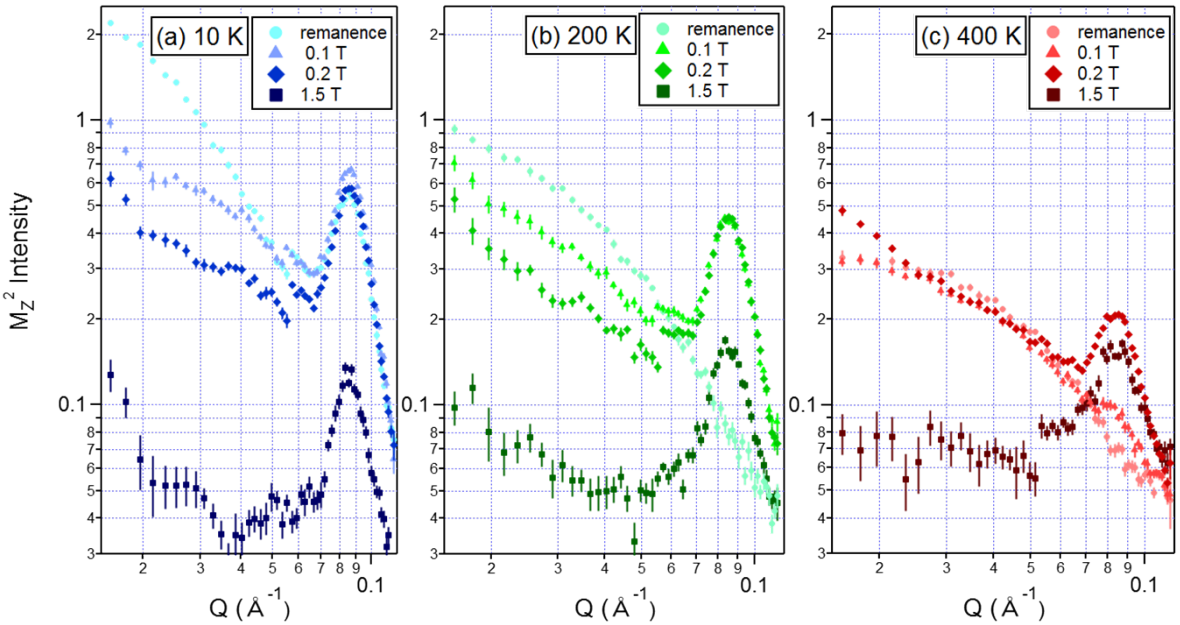

FIG. 6. (Color online.) Data for extracted PASANS intensity M_Z^2 (perpendicular to field direction) using Eqn. 7 vs. scattering vector Q for (a) 10 K (b) 200 K and (c) 400 K with circles for remanent fields, triangles for 0.1 T, diamonds for 0.2 T, and squares for 1.5 T. Error bars in the plot denote standard uncertainties.

presumably as the adopted spin morphology changes length scales as well. This is consistent with the two-component nature of the perpendicular magnetic scattering displayed in Fig. 6, with long-range correlations apparent in the vicinity of the interparticle peak ($\sim 0.085\mathring{A}^{-1}$) and single particle or short-range correlations particularly evident in the low Q range.

The ratio values here are suggestive of non-isotropic, asymmetric spin structures as observed in related Fe_3O_4 assemblies with a magnetic core-shell structure[10]. Note that in other systems where either dipolar or Dzyaloshinskii-Moriya interactions are important, micromagnetic simulations of the expected magnetic Fourier transform components show significant anisotropies[14,40].

IV. IV. MODELING AND DISCUSSION

The PASANS data in Section III reveal two striking magnetic features with significant field and temperature dependence: (1) a magnetic interparticle peak in M_Z^2 and (2) anomalies in the Q-dependent spin flip scattering ratio. Under the same conditions, as shown in

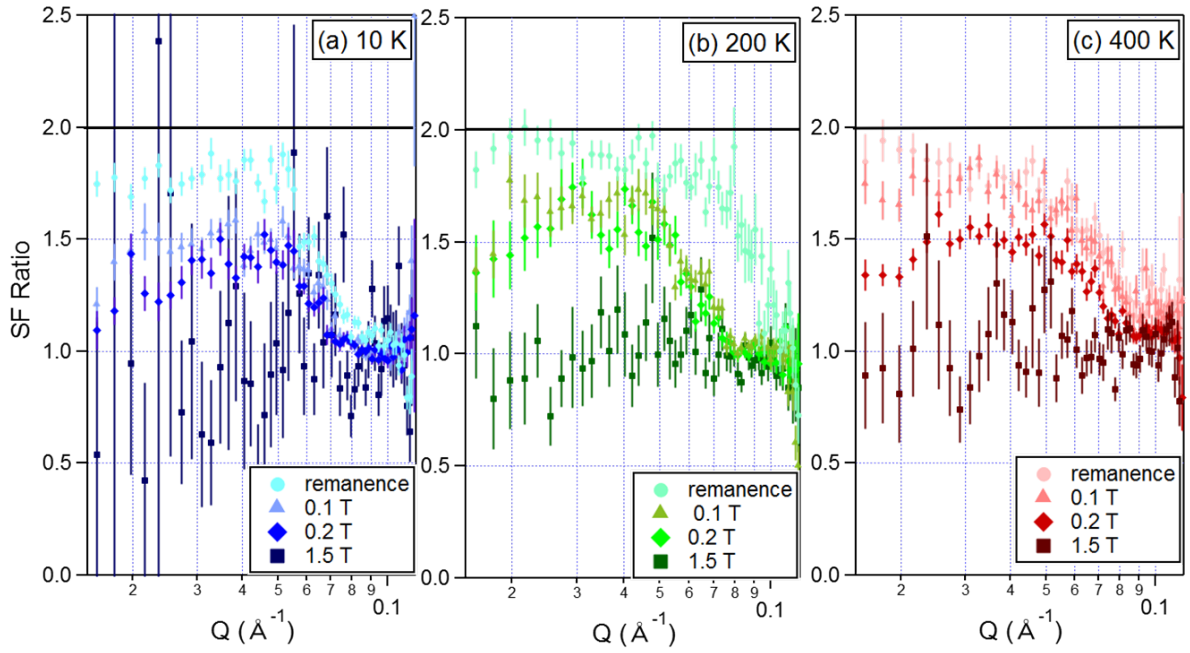

FIG. 7. (Color online.) Spin flip horizontal to vertical scattering ratio (SFR) defined in Eqn. 9 as a function of Q for (a) 10 K (b) 200 K and (c) 400 K with squares for 1.5 T, diamonds for 0.2 T, triangles for 0.1 T, and circles for remanent fields. Error bars in the plot denote standard uncertainties.

the supplementary material, the structural features remain nearly constant, excluding a softening at 400 K for the surfactant coating becoming more fluid-like. These differences indicate that the extent of interparticle magnetic correlations does not simply match the structural ordering. Thus, to explain the variable magnetic characteristics, we construct a model beginning with the known assembly of the close-packed particles and adding the expected dominant dipolar energetics driving the magnetic ordering.

In our three dimensional nanoparticle crystals, dipolar interactions are anticipated to be strongest within a close-packed assembly plane, but weakened along the layer stacking direction which can be subject to stacking faults. We assume an FCC stacking of successive layers in agreement with microscopy observations of the nanocrystallite ordering. We note that in earlier microscopy studies of thin layers of ordered Fe nanoparticles, the preferred moment orientation was found to be very sensitive to layer number, affecting whether the orientation from layer to layer was ferromagnetic in the plane or even possibly antiferromagnetic[41]. Hence, it seems reasonable to explicitly consider the effect of stacking faults on the resulting

magnetic structure in the otherwise ordered nanocrystals.

Within a given close-packed assembly plane, we model any defects or disorder to match the observed structural configuration, as discussed in the supplementary material[38]. Considering the diffraction and neutron magnetic selection conditions, we note this can be accomplished by preferentially favoring the six-fold symmetry axes in the plane as indicated in Fig. 1(c), thereby mimicking anisotropy directions from particle to particle. Note that this is also consistent with the very soft magnetic behavior demonstrated by the particles in Fig. 2; from this, we would expect magnetization to lie in the close-packed planes rather than out of plane along the stacking direction.

From the structural and magnetic data, other possible magnetic interactions are expected to be less significant. The average edge-to-edge nanoparticle separation distance is ~ 1.0 nm, consistent with a lattice spacing of 12 nm, such that direct exchange or superexchange should be weak. In comparison to the very high value for $CoFe_2O_4$[8], magnetocrystalline anisotropy energy in the present system should not dominate as much, being reduced by at least one and nearly two orders of magnitude. The bulk $MnFe_2O_4$ anisotropy value at room temperature is roughly 1/3-1/2 of that for Fe_3O_4 but increases in magnitude with decreasing temperature in contrast to the temperature dependence for bulk Fe_3O_4 approaching the Verwey transition[42]. As a result of these opposing trends, these core-shell $Fe_3O_4/Mn_xFe_{3-x}O_4$ particles are expected to show fewer changes in anisotropy-driven effects with temperature in comparison to the pure Fe_3O_4 system. While we have considered the Dzyaloshinskii-Moriya term explicitly for *intraparticle* spin structures due to symmetry-breaking at the nanoparticle surface[7], it is not clear how such interactions would manifest themselves in the *interparticle* spin structures in our macroscopically homogeneous, polycrystals of nanoparticles.

With these energy considerations in mind, we thus construct a model with an assembly of two-dimensional magnetic "flakes" or plates (Fig. 1(b)), comprised of a cluster of close-packed particles with given magnetic radius, magnetic scattering length density, and fixed separation, bounded by known values from the stoichiometry and physical size. Each magnetic plate consists of a specified number of scattering centers (19 are shown in the Fig. 1(b) schematic) and a fitted number of stacked layers (typically 5) that are offset to preserve the packing and limited to keep the total shape physically plausible. Within a given layer, the in-plane projection of the magnetic moments of all the scattering centers are assumed to point along a hexagonal symmetry direction from nanoparticle to nanoparticle, as illus-

trated in Fig. 1(c) by six-fold in-plane arrows. We consider two possibilities: (1) a random selection of one of these axes in the absence of any magnetic correlations or (2) selection of an easy symmetry axis closest to the applied field direction (indicated in Fig. 1(c) by yellow bolded arrows) in the presence of strong magnetic correlations. Finally, the angle of the magnetization ($\vec{M}$) relative to the in-plane easy direction is selected by minimizing the dipolar coupling energy of the cluster and the Zeeman energy ($-\vec{M} \cdot \mu_o \vec{H}$). This constraint assumes that the magnetization initially lies within the close-packed plane of the plate in low fields (one of the symmetry axes) but tips up out of the plane toward the field direction (X) as the field is increased (Fig. 1(c)). Note that due to dislocations and stacking faults, the magnetic coherence from layer to layer is allowed to vary; in addition, we assume some individual particle moments will not be part of a cluster and allow this free particle fraction to vary. A fixed volume fraction based on sample size sets the scaling for the simulated scattering, along with a fixed flat background term. In this fashion, regions or domains for possible magnetic scattering can be constructed.

The plates are rotated over all possible orientations, as indicated by angles ψ, ω, and Φ in Fig. 1(c) to account for the fact that the clusters are assumed to be randomly arranged in space. The contributions to the scattering are then computed, making use of the relevant selection rules described in[28,29]. The simulated scattering is smeared by the instrumental resolution to compare against the measured experimental data.

Figure 8 shows the important role of the easy symmetry axis selection, considering the specific case of the nanoparticles at 200 K in a magnetic field of 0.1 T with either preferred axis correlation or not. While in either case, the vertical SF data are reasonably well-captured by the modeling, imposition of the nearest-to-field symmetry easy axis choice is necessary to capture the horizontal SF intensity at the interparticle peak, as well as to match the intensity elsewhere to mimic the experimental SF ratio (Figure 9). Removing any symmetry axes in the model at all leads to a degradation of the match to the experimental data, similar to that observed for the case of no axis correlation.

The specific variable parameters for the model with preferred axis correlation for this intermediate field and temperature condition are indicated in[38], with the flake consisting of 37 scattering centers and 5 layers with 25% coherence from layer to layer and magnetic scattering length density and radius under the expected maximum values based on bulk behavior. A 7.5% free particle fraction is assumed. Under these conditions, the balance of

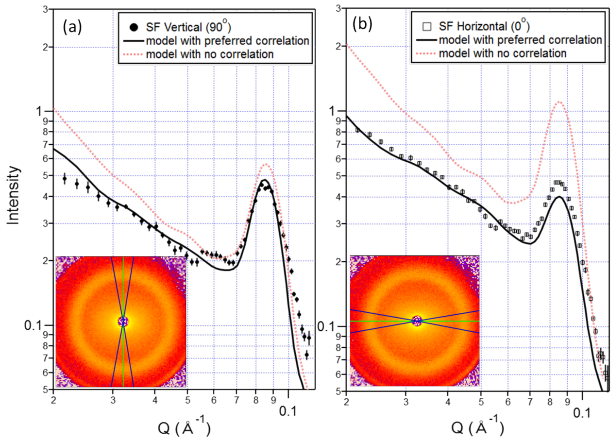

FIG. 8. (Color online.) Simulated spin flip scattering in the (a) vertical ($\theta = \pm 90°$) and (b) horizontal ($\theta = 0°$ or 180°) directions, compared against PASANS data for the $Fe_3O_4/Mn_xFe_{3-x}O_4$ nanoparticle assemblies at 200 K in a magnetic field of 0.1 T. Error bars in the plot denote standard uncertainties. The dotted (red) lines show predicted scattering assuming no correlations and a random selection of the symmetry axis in a close-packed plate, while the solid (black) lines show the same scattering, assuming selection of the axis nearest to the applied magnetic field. All other model parameters are maintained constant, with key values listed in Table S-II of Ref.[38]. Insets indicate the sectors of data that were analyzed.

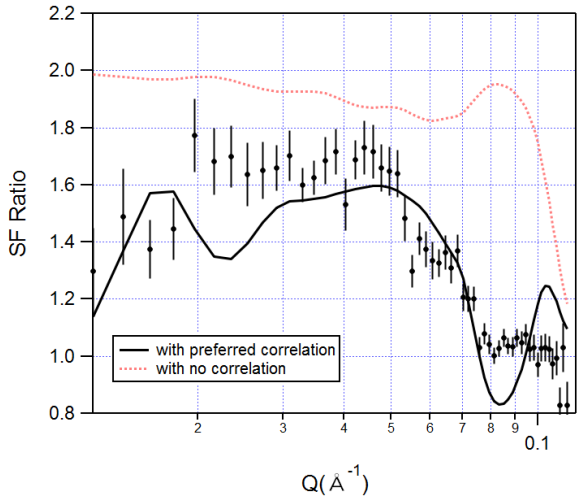

FIG. 9. (Color online.) Simulated spin flip scattering ratio assuming random selection of six-fold symmetry axis for no correlation (dashed red curve) vs. selection of axis nearest to applied field (solid black curve) for preferred correlation, in comparison against experimental data for assemblies at 200 K in a magnetic field of 0.1 T. Error bars in the plot denote standard uncertainties.

the Zeeman energy with the dipole interaction considerations leads to a net magnetization tipped on average 9.5° from the plane.

We have then applied this model approach across the whole set of field and temperature conditions as listed and displayed in the supplementary material[38]. We find that the data sets can be simulated for physically reasonable parameter choices in particular with magnetic radius not exceeding the value expected from the observed particle diameter (7.4 ± 1 nm) within uncertainty and with magnetic scattering length density not higher than the 1.5-1.6 x 10^{-6} $\mathring{A}^{-2}$ expected for Fe_3O_4 and $MnFe_2O_4$ based on bulk magnetization values. The magnetic scattering length density and magnetic radius associated with the scattering centers reach the expected maximal values in higher magnetic field and lower temperature conditions; these conditions are also associated with larger clusters (with more centers and more layers), higher degree of layer alignment, and lower free particle fractions.

To understand the interplay of these parameters in more depth, we plot in Fig. 10(a), the averaged tilt angles for the various model conditions. Note that since a range of all possible flake orientations relative to an applied field is considered, an average tilt angle of 45°, rather than 90°, corresponds to complete field alignment. In Fig. 10(b), to compare these angles against the DC magnetization data in Fig. 2, we consider the magnetization at a particular field value (M_H) relative to the maximum magnetization at 5 T (M_{max}) at a given temperature and compute the corresponding angle θ_{mag} assuming a simple alignment relationship: $\theta_{mag} = sin^{-1}(M_H/M_{max})$.

Overall, the model behaviors at 10 K and 200 K are more similar in comparison to that at 400 K, reflecting the general trends in the magnetic PASANS data for Figs. 4-7. At lower temperatures, the interplay of the energetics favors larger, more plate-like magnetic domains with net magnetization closer to the flake or plate. In this fashion, the PASANS data can be explained in terms of tracking the formation of regions of magnetically-correlated nanoparticles, but with strong preferential alignment of the magnetic moments to symmetry directions in the close-packed plane due to dipolar interactions.

In contrast, at 400 K the parameters for magnetic scattering length density and magnetic radius are reduced, as would be expected from the behavior of bulk $MnFe_2O_4$ at elevated temperature. These reductions should weaken dipolar interactions; with Zeeman energy contributions now more important, the averaged tilt angles increase towards the applied field direction, even in moderate fields of 0.1 to 0.2 T. Consistent with this dipolar interaction

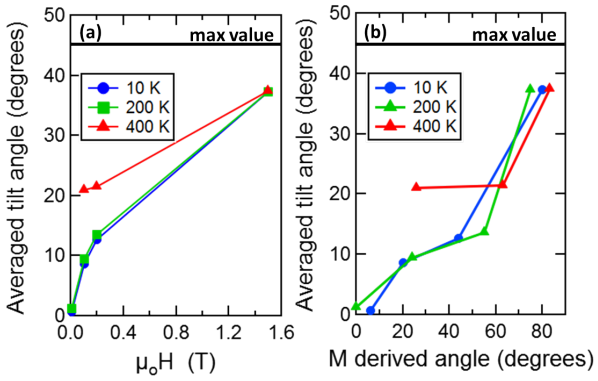

FIG. 10. (Color online.) (a) Averaged tilt angle of the magnetization vs. magnetic field assuming model parameters listed in Table S-II of Ref.[38], with blue circles for 10 K, green squares for 200 K and red triangles for 400 K. Zero degrees corresponds to alignment within the plane of scattering centers. Note at 400 K in remanence, the modeled "cluster" consists only of one scattering center and is thus omitted. (b) Averaged tilt angle of the magnetization vs. derived magnetization tilt angle using magnetization data from Fig. 2. The relationship is nearly linear as expected, at 10 K and 200 K.

weakening, the 400 K data are modeled best by the formation of much smaller, more isotropic clusters relative to the case at 10 K or 200 K. The cluster size change is now a very significant contributor to the overall magnetic behavior with field, such that the relationship of averaged tilt to the magnetometry data is less clear in Fig. 10(b), relative to the lower temperature data which are more linear.

The presence of 2D magnetic plate-like structures for a number of the fields and temperatures is a particularly intriguing feature of the modeled data, especially since the structural extent of the dense nanoparticle assemblies is long-range and 3D, albeit with stacking faults and other defects. To explain this feature, we note that while the energy differences between the arrays as a result of such dislocations are very small, these defects are known to have a possibly dramatic effect on magnetic ordering. As mentioned earlier, in thin films of assembled Fe nanoparticles, magnetic alignment was highly dependent on particle size and thickness, with behavior ranging from ferromagnetic all the way to antiferromagnetic layer coupling[41]. More recent work on ordered collections of γ-Fe_2O_3 nanoparticles[15] has explicitly probed the crossover from 2D to 3D-like structures, centered on the formation of flux closure or vortex states which vary in orientation depending on thickness. As might be expected,

more 3D-like character is found for increasing thickness, but even for their bulk case with a thickness of a few μm and hence comparable to our nanocrystals, isotropic magnetic behavior is *not* observed – an effect attributed to deviations from perfect FCC structure. This matches on to our results here, although it is more difficult to compute the specific energetics in our system given a collection of defected grains vs. focusing on just one. In comparison to[15], we note that these core-shell nanoparticles are significantly softer magnetically with pronounced temperature dependence to the magnetization as shown in Fig. 2. Hence, it seems very plausible for the dipolar interactions coupled to the defected structure to favor 2D-like magnetic domains for some range of field and temperature conditions.

Ultimately, the 2D magnetic behavior may stem from the nature of the defects and stacking faults created in the assembly process. While in our case, we are unable to determine the exact nature of the ordered regions within the interior of the 3D assemblies, we note that for CdSe nanoparticles self-assembled in a similar fashion, thin hexagonal platelets were formed and directly imaged[31]. Thus, one possibility is that our 3D assemblies consist of stackings of different thin platelets, giving rise quite naturally to the 2D magnetic flake behavior.

V. V. SUMMARY AND CONCLUSIONS

In summary, we have used advanced PASANS methods to directly probe the spin structures in ordered $Fe_3O_4/Mn_xFe_{3-x}O_4$ nanoparticle assemblies with a three-dimensional character. In a variety of field and temperature conditions, we observe a significant perpendicular magnetic scattering signal that is coherent from nanoparticle to nanoparticle; we outline a general procedure to perform the polarization correction in the vicinity of this magnetic Bragg peak[38]. The longer-range magnetic correlations in this system manifest themselves in a range of SF scattering ratios as well. In contrast to other work, we explicitly determine experimental length scales for these correlations.

Overall, the field and temperature trends in the PASANS data are captured by a model which highlights the competition between the dipolar interactions among the nanoparticles and the Zeeman energy in a field, with preferred net spin alignment relative to pre-existing packing symmetry axes. The 2D plate-like magnetic structures appear to stem from the combination of very soft magnetic particles and the presence of stacking faults and related

small structural defects. Note the model does not include or require details of the magnetic structure within each single nanoparticle, relying instead on relatively small net changes in magnetic radius and magnetic scattering length density to capture what is likely a complicated intraparticle configuration. In our earlier investigation, we performed atomistic calculations that consider in detail the nature of Heisenberg exchange or other possible contributing interactions such as a Dzyaloshinskii-Moriya term[7] in our core/shell nanoparticles. The calculations show that the contribution of both of these factors govern spin canting within a single particle, although these computationally-intensive calculations could not be extended to an ensemble of nanoparticles which have relatively complex chemical structure. Nanoparticles with homogeneous $MnFe_2O_4$ composition would clearly have been preferable from a modeling standpoint, but only if the size uniformity and ability to order into 3D crystals remain intact; the synthesis method described in[5,7] is very successful for ordering, albeit with core-shell particles formed in the precursor decomposition process. Further improvements to the model could be achieved by including distributions of plate or cluster size, which are undoubtedly present in the sample. Nevertheless, the results here indicate that the relatively small changes in individual particle net moment at different temperatures and fields are amplified in the collective magnetic behavior of our nanoparticle ensemble which is strongly influenced by dipolar interactions.

The spin structures adopted in these $Fe_3O_4/Mn_xFe_{3-x}O_4$ nanoparticle assemblies represent yet a different solution to competing energetics in comparison to our earlier studies on $CoFe_2O_4$ and Fe_3O_4[8–10]. For $CoFe_2O_4$ assemblies, the very high magnetocrystalline anisotropy along with Zeeman energy in a field provide the dominant considerations for controlling what is mostly a single particle alignment. In the Fe_3O_4 assemblies, exchange and Zeeman energies were the dominant terms, but with magnetocrystalline anisotropy and dipolar interactions shaping the energy landscape; these nanoparticles were structurally uniform but with a magnetic core and shell that changed with field and temperature. For the current system, changes in the intraparticle magnetic structure were more modest[7], consistent with the anticipated reduced exchange in manganese ferrite vs. magnetite based on the Curie temperature and the moderated anisotropy based on averaging the bulk values for $MnFe_2O_4$ and Fe_3O_4. In this case, the remaining consideration of dipolar interactions clearly plays an increasingly important role in determining the unique, two-dimensional nature of the collective magnetic order.

These results are significant, given the many applications that rely on a high concentration of magnetic nanoparticles, with either explicit or implicit assumptions as to the governing spin morphologies. From an experimental technique standpoint, the power of the PASANS method is highlighted and further extended to properly account for the possible difference in sample depolarization in the vicinity of a magnetic Bragg reflection. The data and analysis shown here provide further evidence of the wide range of magnetic nanoparticle spin structures that may be adopted, depending on the delicate balance of the competing energetics in the composite systems.

ACKNOWLEDGMENTS

We thank W.C. Chen and S.M. Watson for their assistance with the polarized ^{3}He spin filters. Access to the filters on the NG7 SANS instrument at the NIST Center for Neutron Research was provided by the Center for High Resolution Neutron Scattering, a partnership between the National Institute of Standards and Technology and the National Science Foundation (NSF) under DMR-1508249. This work was also partially supported by NSF DMR-1606887 and an Oberlin College Research Status Award. S. D. Oberdick, A. Adbdelgawad, and S. A. Majetich further acknowledge support by the Department of Energy through grants #DE-FG02-08ER46481 and #DE-SC0019237.

---

* yumi.ijiri@oberlin.edu

[1] Z. Z. Bandic and R. H. Victora, Proc. IEEE **96**, 1749 (2008).

[2] K. Krishnan, IEEE Trans. Magn. **46**, 2523 (2010).

[3] S. A. Majetich, T. Wen, and O. T. Mefford, MRS. Bull. **38**, 899 (2013).

[4] A. López-Ortega, M. Estrader, G. Salazar-Alvarez, S. Estradé, I. V. Golosovsky, R. K. Dumas, D. J. Keavney, M. Vasilakaki, K. N. Trohidou, J. Sort, F. Peiró, S. Suriñach, M. D. Baró, and J. Nogués, Nanoscale **4**, 5138 (2012).

[5] X. Sun, A. Klapper, Y. Su, K. Nemkovski, A. Wildes, H. Bauer, O. Köhler, A. Schilmann, W. Tremel, O. Petracic, and T. Brückel, Phys. Rev. B **95**, 134427 (2017).

[6] C. Liu, B. Zou, A. Rondinone, and Z. J. Zhang, J. Phys. Chem. B **104**, 1141 (2000).

[7] S. D. Oberdick, A. Abdelgawad, C. Moya, S. Mesbahi-Vasey, D. Kepaptsoglou, V. K. Lazarov, R. F. L. Evans, D. Meilak, E. Skoropata, J. van Lierop, I. Hunt-Isaak, H. Pan, Y. Ijiri, K. L. Krycka, J. A. Borchers, and S. Majetich, Sci. Rep. **8**, 3425 (2018).

[8] K. Hasz, Y. Ijiri, K. L. Krycka, J. A. Borchers, R. A. Booth, S. Oberdick, and S. A. Majetich, Phys. Rev. B **90**, 180405(R) (2014).

[9] K. L. Krycka, R. A. Booth, C. R. Hogg, Y. Ijiri, J. A. Borchers, W. C. Chen, S. M. Watson, M. Laver, T. R. Gentile, L. R. Dedon, S. Harris, J. J. Rhyne, and S. A. Majetich, Phys. Rev. Lett. **104**, 207203 (2010).

[10] K. L. Krycka, J. A. Borchers, R. A. Booth, S. A. Majetich, Y. Ijiri, K. Hasz, and J. J. Rhyne, Phys. Rev. Lett. **113**, 147203 (2014).

[11] S. Chikazumi, *Physics of Ferromagnetism* (Oxford University Press, 1997).

[12] C. Nisoli, R. Moessner, and P. Schiffer, Rev. Mod. Phys. **85**, 1473 (2013).

[13] D. B. A. Browaeys and T. Lahaye, J. Phys. B **49**, 152001 (2016).

[14] S. Erokhin, D. Berkov, and A. Michels, Phys. Rev. B **92**, 014427 (2015).

[15] B. Faure, E. Wetterskog, K. Gunnarsson, E. Josten, R. P. Hermann, T. Bruckel, J. W. Andreasen, F. Meneau, M. Meyer, A. Lyubartsev, L. Bergstrom, G. Salazar-Alvarez, and P. Svedlindh, Nanoscale **5**, 953 (2013).

[16] P. Bender, E. Wetterskog, D. Honecker, J. Fock, C. Frandsen, C. Moerland, L. K. Bogart, O. Posth, W. Szczerba, H. Gavilán, R. Costo, M. T. Fernández-Díaz, D. González-Alonso, L. Fernández-Barquín, and C. Johansson, Phys. Rev. B **98**, 224420 (2018).

[17] P. Hugounenq, M. Levy, D. Alloyeau, L. Lartigue, E. Dubois, V. Cabuil, C. Ricolleau, S. Roux, C. Wilhelm, F. Gazeau, and R. Bazzi, J. Phys. Chem. C **116**, 1570215712 (2012).

[18] R. Fu, Y. Yan, C. Roberts, Z. Liu, and Y. Chen, Sci. Rep. **8**, 4704 (2018).

[19] M. E. F. Brollo, P. H. Flores, L. Gutiérrez, C. Johansson, D. F. Barber, and M. P. Morales, Phys. Chem. Chem. Phys. **20**, 17829 (2018).

[20] A. Wiedenmann, J. Appl. Cryst. **33**, 428 (2000).

[21] I. Bergenti, A. Deriu, L. Savini, E. Bonetti, F. Spizzo, and H. Hoell, J. Magn. Magn. Matl. **262**, 60 (2003).

[22] S. M. Yusuf, J. M. DeTeresa, M. D. Mukadam, J. Kohlbrecher, M. R. Ibarra, J. Arbiol, P. Sharma, and S. K. Kulshreshtha, Phys. Rev. B **74**, 224428 (2006).

[23] N. A. Grigorieva, S. V. Grigoriev, H. Eckerlebe, A. A. Eliseev, K. S. Napolskii, A. V. Lukashin,

and Y. D. Tretyakov, J. Magn. Magn. Matl. **300**, e342 (2006).

[24] T. Oku, T. Kikuchi, T. Shinohara, J. Suzuki, Y. Ishii, M. Takeda, J. Kakurai, Y. Sasaki, M. Kihsimoto, M. Yokoyama, and Y. Nishihara, Physica B **404**, 2575 (2009).

[25] K. Theis-Bröhl, M. Wolff, I. Ennen, C. D. Dewhurst, A. Hütten, and B. P. Toperverg, Phys. Rev. B **78**, 134426 (2008).

[26] P. K. Manna, S. M. Yusuf, M. D. Mukadam, and J. Kohlbrecher, Appl. Phys. A **109**, 385 (2012).

[27] K. L. Krycka, J. A. Borchers, M. Laver, G. Salazar-Alvarez, A. López-Ortega, M. Estrader, S. Suriñach, M. D. Baró, J. Sort, and J. Nogués, J. Appl. Phys. **113**, 17B531 (2013).

[28] R. M. Moon, T. Riste, and W. C. Koehler, Phys. Rev. **181**, 920 (1969).

[29] K. L. Krycka, J. Borchers, Y. Ijiri, R. A. Booth, and S. Majetich, J. Appl. Cryst. **45**, 554 (2012).

[30] D. Honecker, A. Ferdinand, F. Döbrich, C. D. Dewhurst, A. Wiedenmann, C. Gómez-Polo, K. Suzuki, and A. Michels, Eur. Phys. J. B **76**, 209 (2010).

[31] D. V. Talapin, E. V. Shevchenko, A. Kornowski, N. Gaponik, M. Haase, A. L. Rogach, and H. Weller, Advanced Materials **13**, 1868 (2001).

[32] D. F. Farrell, Y. Ijiri, C. V. Kelly, J. A. Borchers, J. J. Rhyne, Y. Ding, and S. A. Majetich, J. Magn. Magn. Mater **303**, 318 (2006).

[33] D. Farrell, Y. Chen, S. Kan, M. Sachan, Y. Ding, S. A. Majetich, and L. Yang, J. Phys. Conf. Ser. **17**, 185 (2005).

[34] S. A. Majetich and M. Sachan, J. Phys. D **39**, R407 (2006).

[35] K. L. Krycka, R. Booth, J. A. Borchers, W. C. Chen, C. Conlon, T. R. Gentile, C. Hogg, Y. Ijiri, M. Laver, B. B. Maranville, S. A. Majetich, J. J. Rhyne, and S. M. Watson, Physica B **404B**, 251 (2009).

[36] W. C. Chen, R. Erwin, J. W. M. III, S. Watson, C. B. Fu, T. R. Gentile, J. A. Borchers, J. W. Lynn, and G. L. Jones, Physica B **404B**, 2663 (2009).

[37] K. L. Krycka, W. Chen, J. Borchers, B. Maranville, and S. Watson, J. Appl. Cryst. **45**, 546 (2012).

[38] See supplemental material at http://link.aps.org/supplemental/XXXX for 1) additional details on polarization correction, 2) features of the structural data, and 3) complete model information for the data sets at different temperature and field conditions.

[39] A small field is necessary to maintain neutron beam polarization, but given the magnetization data in Fig. 2, the remanent field should approximate true zero.

[40] A. Michels, D. Mettus, D. Honecker, and K. L. Metlov, Phys. Rev. B **94**, 054424 (2016).

[41] S. Yamamuro, D. F. Farrell, and S. A. Majetich, Phys. Rev. B **65**, 224431 (2002).

[42] N. Miyata, J. Phys. Soc. Japan **16**, 1291 (1961).